Parametric Numerical Study on the Performance Characteristics of a Micro-Wave Rotor Gas Turbine

Stefan Tüchler[1], Colin D. Copeland[1]

Abstract— In this paper, an alternative micro-gas turbine is proposed, where the traditional compressor-turbine arrangement is replaced by an axial, throughflow wave rotor. The investigated wave rotor features symmetrically cambered wall profiles and angled port arrangement for shaft power extraction and uses shock and rarefaction waves for pressure exchange and to achieve gas compression and expansion within a single device.

A validated quasi-one-dimensional model that solves the laminar Navier-Stokes equations using a two-step Richtmyer TVD scheme with minmod flux limiter is employed to characterise and examine micro-gas turbine behaviour. The model accounts for wall heat transfer, flow leakage, wall friction and inviscid blade forces. In addition, modified boundary conditions consider finite passage opening effects and a simple steady-flow combustor model is defined that links the high pressure in- and outlet ports.

The model is used to conduct a parametric study to investigate the effects of leakage gap, heat release rate, exhaust backpressure, as well as profile camber on gas turbine performance with a focus on generated combustor compression and expansion efficiency, shaft power and system efficiency. The implications of combustor pressure loss as well as effects of a potential recuperator are discussed as well. The results identify axial leakage and combustor pressure loss as primary drivers for enhanced performance. Finally, the results reinforce the capacity of wave rotors to compress and expand gas efficiently, while thermal efficiency remains below 10 percent.

Nomenclature

Variables

$\dot{m}$	Mass flow rate [kg/s]
$\dot{Q}$	Rate of heat flow [W]
$\mathbf{F}$	Flux vector
$\mathbf{S}$	Source term vector
$\mathbf{U}$	State vector
C_D	Discharge coefficient [-]
c_p	Specific heat capacity at const. pressure [J/kg-K]
c_v	Specific heat capacity at const. volume [J/kg-K]
A	Cross-sectional area [m^2]
a	Speed of sound [m/s]
C	Absolute velocity [m/s]
D	Diameter [m]
e	Specific internal energy [J/kg]
f	Friction factor [-]
H	Channel height [m]
h	Specific enthalpy [J/kg]
htc	Convective heat transfer coefficient [W/m^2-K]
k	Surface roughness [m]
L	Length [m]
m	Mass [kg]
Nu	Nusselt number [-]
P	Power [W]
p	Pressure [Pa]
Pr	Prandtl number [-]
q	Heat flux [W/m^2]
R	Specific gas constant [J/kg-K]
r	Radius [m]
Re	Reynolds number [-]
S	Wetted area [m^2]
s	Specific entropy [J/kg-K]
T	Temperature [K]
T	Volume [m^3]
t	Time [s]
u	Relative velocity [m/s]
x,z	Cartesian coordinates

Sub- and Superscripts

ax	Axial
b	Blade
c	Cold, compression
cav	Leakage cavity
cc	Combustion chamber
ch	Channel
f	Friction
h	Hot, hydraulic
hr	Heat release
i	In
int	Interface
is	Isentropic
lk	leakage
o	Out
p	Penetration
s	Static
t	Total
TT	Total-to-total
w	Wall
x	Expansion

Abbreviations

EGR	Exhaust gas recirculation
FAE	Fresh air exhaustion
HPA	High pressure air
HPG	High pressure gas
LPA	Low pressure air
LPG	Low pressure gas
OPL	Overall pressure loss
TVD	Time variation diminishing

[1]Powertrain and Vehicle Research Centre (PVRC), Department of Mechanical Engineering, University of Bath, Bath, Claverton Down, Bath BA2 7AY, United Kingdom S.Tuechler@bath.ac.uk, C.D.Copeland@bath.ac.uk

Greek Symbols

β	Blade angle [°]
δ	Axial leakage gap [m]
η	Efficiency [-]
γ	Ratio of specific heats [-]
λ	Loop flow ratio [-]
μ	Dynamic viscosity [kg/m-s]
ω	Angular speed [rad/s]
Π	Pressure ratio [-]
Ψ	EGR/FAE rate [-]
ρ	Density [kg/m^3]
τ	Time constant [s]
Θ	Leakage function
θ	Azimuth angle [°]
ζ	Loss coefficient [-]

I. INTRODUCTION

A. Background

Over the past years, a growing demand for robotic and autonomous systems in both the civilian and defence market has developed. Applications range from unmanned aircraft systems to autonomous marine robots and mobile power packs used in the military [1]. These devices need to be compact and require energy dense power sources in order to operate continuously for several hours or days. At present, battery systems fail to meet these requirements due to their low energy density and the large volume required for installation [2].

Gas turbines on the other hand excel at high specific energy and power density [3]. Moreover, they are a well established technology, compact in size, reliable and can accommodate various types of fuels [4]. However, the performance of gas turbines is significantly affected by downsizing. In particular, downscaling a given design to match a certain set of requirements for lower power output entails substantial performance penalties pertaining to efficiency, design and operation. To maintain similar enthalpy levels and pressure changes it is necessary to run at considerably larger rotational speeds to the detriment of reliability. Heat transfer between hot and cold parts becomes more pronounced the smaller the unit size [5]. Also, tip leakage losses increase along with frictional losses due to larger relative surface roughness. All these factors combined contribute to a decline in both component efficiencies and thermal efficiency [6]–[8].

Substituting compressor and turbine in a standard gas turbine arrangement, given in Figure 1(a), by a wave rotor unit, as shown in Figure 1(b), allows to combine compression, expansion and shaft power generation within a single device and can potentially mitigate several of the aforementioned shortcomings. One distinct advantage of such an unsteady flow device over steady (e.g. diffusers) or crypto-steady flow devices is a high compression efficiency and that compression can occur within a compact volume. Since the port arrangement is a function of the circumferential velocity, it is possible to run the wave rotor at considerably lower speeds than turbomachinery of comparable size, with the result of making it less susceptible to high speed fatigue.
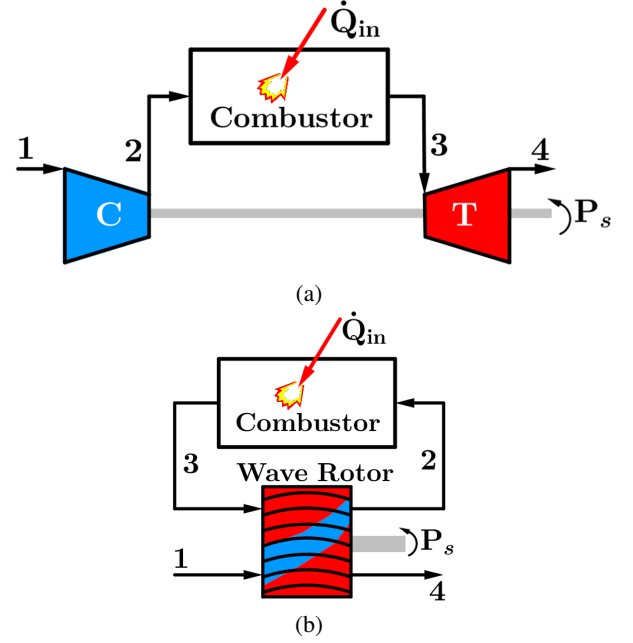

Fig. 1: (a) depicts a schematic for an unrecuperated gas turbine consisting of axial or radial compressor connected via a shaft to a turbine and a combustor in between. (b) The wave rotor concept combines both features in one device. It houses two streams, namely cold air being compressed by means of shock compression and directed to the combustor while a hot gas stream is expanded through a series of expansion waves and expelled to the ambience.

Finally, exposure to hot and cold gases introduces a certain level of self-cooling capacity that potentially allows to run at a higher combustor outlet temperatures.

The wave rotor is an unsteady flow device that relies on exchange of energy through shock and expansion waves and consists of an array of channels or passages aligned along a cylindrical drum, shown in Figure 2(a). To each side of the spinning rotor, stator endplates are located that house port openings connected to in- and outlet manifolds and the combustor. Unfolding the circumference and plotting the wave pattern and temperature distribution on a two-dimensional θ-z-plane results in the schematic presented in Figure 2(b). Exposing the channel to the left with the high pressure, high temperature exhaust gas from the combustor outlet port (high pressure gas-HPG) sets off a right travelling, primary shock wave (S1). Upon reaching the other end of the channel the high pressure air (HPA) port is opened and the shock wave is reflected resulting in a secondary, left running shock wave (S2). These two shock waves compress the incoming fresh air and essentially represent the work done by a compressor in the traditional gas turbine.

Closing the HPG port sparks an expansion fan or rarefaction wave (R1), which expands the exhaust gases to an intermediate pressure level. Impingement of the head of R1 on the right hand side marks the closure of the HPA port, which brings about a hammer shock. Opening the low
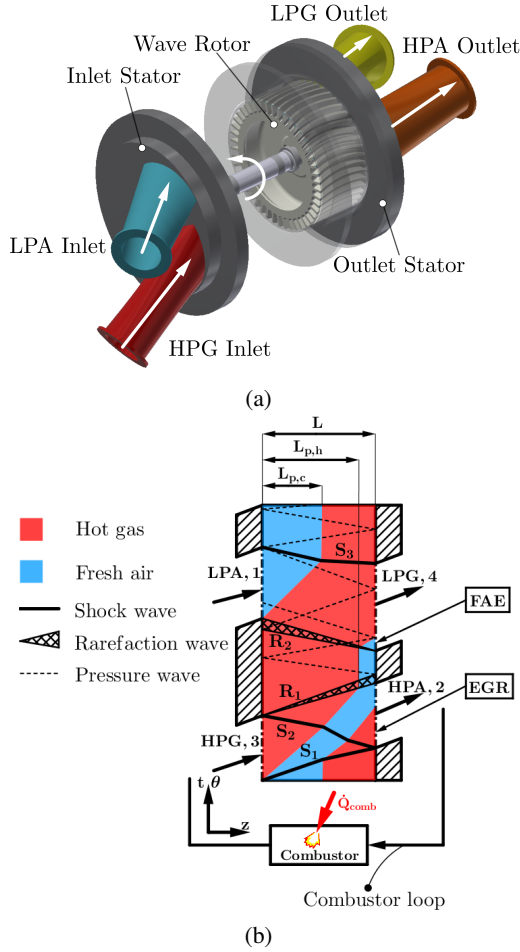
Fig. 2: (a) Main components of a generic four-port, single cycle throughflow wave rotor consisting of inlet and outlet stator endplates and rotor/bearing assembly. (b) Unfolded view of the wave pattern experienced as a single channel passes through the port arrangement of a four-port through-flow wave rotor showed in the θ-z plane [9].

air from the ambience without any upstream pressurisation. Equally, if pressure and temperature in the HPG duct drop below a certain threshold, it is possible that the hot gas penetration length $L_{p,h}$ does not reach the HPA port, leading to fresh air exhaustion (FAE). While a certain percentage of EGR can potentially have favourable effects with respect to combustion and emission characteristics, FAE is generally an undesirable effect, as it represents air being compressed and subsequently expelled without being further used throughout the cycle.

B. Literature Survey

Wave rotors have been proposed as a means of enhancing thermodynamic cycles for a large spectrum of applications, showing promising results potential in gas turbine topping cycles [10], [11], supercharging of internal combustion engines [12]. More recently, there has been a renewed interest in wave rotor applications for constant-volume combustors [13]–[15] and refrigeration cycles [16], [17].

One of the earliest applications of wave rotors focused on the development of a wave rotor engine [18]–[22]. Weber's shock wave engine concept [18] was an axial, single-cycle, throughflow device with angled blades for shaft power extraction combined with classical turbomachinery. Cycle efficiency of the entire system was predicted to be in the range of 29% to 36%. While Weber's proposed engine remained a concept, General Electric and General Power Corporation designed and built a wave engine that was experimentally tested, but failed to produce the predicted power output. This lead to suspension of the project. Pearson's wave engine [19], [20] encompassed a rotor of approximately 230 mm in diameter with a design speed of 18,000 rpm and produced up to 26 kW at design conditions, where thermal efficiency varied between 4-9%. Recently, a radial wave disk engine concept was introduced by Michigan State University and Warsaw University of Technology [23]–[25] for sub 1kW shaft power output. Computational fluid dynamics simulations in one- [23] and two-dimensions [25] were carried out showing a two-step compression system thermal efficiency of approximately 13-16% and 10% respectively, while a single-compression system would merely operate at 2% [24] at the benefit enhanced operation stability.

This paper seeks to investigate the characteristics of a small scale wave rotor gas turbine through a parameteric study. The foundations of the study are a throughflow wave rotor with symmetrically cambered wall profiles previously characterised experimentally [9] and a validated quasi-one-dimensional numerical model that accounts for wall friction, flow leakage, wall heat transfer, inviscid blade forces [26]. The study examines the effects of inlet mass flow ratio (i.e. loop flow ratio), heat addition, exhaust backpressure, leakage, combustor pressure loss, camber profile and recuperation on wave rotor performance with a focus on thermal efficiency, adiabatic efficiencies, power output and combustor temperature.

pressure exhaust port (LPG) leads to further expansion of the gases (R2) before the gases are ejected to the ambience. The low pressure inlet port opens as soon as (R2) reaches the left hand side of the channel. Finally, the closure of the LPG port generates another (relatively weak) shock wave (S3), which is further reflected and attenuated on the channel sides before the cycle is repeated.

An intrinsic feature of throughflow wave rotors is internal exhaust gas recirculation (EGR), as pointed out Figure 2(b). The amount of EGR is foremost a function of the fresh air scavenging achieved through opening of the LPA port. The higher the penetration length $L_{p,c}$, the higher the amount of exhaust gases expelled through the LPG port. In effect, $L_{p,c}$ is governed by the mass flow imbalance between the high and low pressure inlet ports. Defining the mass flow or loop flow ratio of high- to low pressure inlet as $\lambda = \dot{m}_{HPG}/\dot{m}_{LPA}$ gives a measure of this mass flow imbalance. The loop flow ratio is generally >1, in particularly for cases where LPA draws

II. METHODOLOGY

A. Numerical Quasi One-Dimensional Model

1) Governing Equations: The model is based on the one-dimensional compressible and unsteady Navier-Stokes equation defined as

$$\frac{\partial \mathbf{U}}{\partial t} + \frac{\partial \mathbf{F}(\mathbf{U})}{\partial z} = \mathbf{S} \tag{1}$$

where the state vector takes the form

$$\mathbf{U} = \begin{pmatrix} \rho \\ \rho u \\ \rho E \end{pmatrix} \tag{2}$$

while the flux vector is defined as

$$\mathbf{F} = \begin{pmatrix} \rho u \\ \rho u^2 + p - \tau_{zz} \\ \rho u \left(E + \dfrac{p}{\rho} - \tau_{zz} + q_z \right) \end{pmatrix} \tag{3}$$

Heat flux is given by Fourier's law and viscous stress simplified through Stokes' hypothesis to yield

$$q_z = -k \frac{\partial T}{\partial z}, \qquad \tau_{zz} = \frac{4}{3} \mu \frac{\partial u}{\partial z} \tag{4}$$

Model closure is achieved through the ideal gas equation, stating $p=\rho RT$. Air is treated as a calorically imperfect gas with specific heat capacity being a function of temperature, that is $c_p=f(T)$. The right hand side of Equation 1 denotes the source vector that accommodates for wall friction, wall heat transfer, inviscid profile forces and losses as well as flow leakage between the rotor and the stators.

2) Discretisation Scheme: The flow equations of Equation 1 are integrated explicitly in time using a two-step second-order accurate scheme of Richtmyer with a TVD scheme using a Roe and Baines minmod flux limiter. The first step consists of a first-order Lax-Friedrichs method, while the following second step represents a mid-point Leapfrog approach. The resulting algebraic equations are given in Equation 5 and 6.

$$\mathbf{U}_{i+1/2}^{n+1/2} = \frac{1}{2} \left(\mathbf{U}_{i+1}^n + \mathbf{U}_i^n \right) - \frac{\Delta t}{2\Delta z} \left(\mathbf{F}_{i+1}^n - \mathbf{F}_i^n \right)$$
$$- \frac{\Delta t}{4} \left(\mathbf{S}_{i+1}^n - \mathbf{S}_i^n \right)$$
$$\mathbf{U}_{i-1/2}^{n+1/2} = \frac{1}{2} \left(\mathbf{U}_i^n + \mathbf{U}_{i-1}^n \right) - \frac{\Delta t}{2\Delta z} \left(\mathbf{F}_i^n - \mathbf{F}_{i-1}^n \right)$$
$$- \frac{\Delta t}{4} \left(\mathbf{S}_i^n - \mathbf{S}_{i-1}^n \right) \tag{5}$$

$$\mathbf{U}_i^{n+1/2} = \mathbf{U}_i^n - \frac{\Delta t}{\Delta z} \left(\mathbf{F}_{i+1/2}^{n+1/2} - \mathbf{F}_{i-1/2}^{n+1/2} \right)$$
$$- \frac{\Delta t}{2} \left(\mathbf{S}_{i+1/2}^{n+1/2} - \mathbf{S}_{i-1/2}^{n+1/2} \right) \tag{6}$$

The time step is chosen adaptively based on the maximum wave speed within the domain $\max\limits_{i}(|u_i^n| + a_i^n)$ and a fixed Courant number of 0.7 [27].

3) Boundary Conditions: In this study, boundary conditions are implemented through a cell-centred approach with fictitious cells outside of the domain boundaries, as shown in Figure 3.
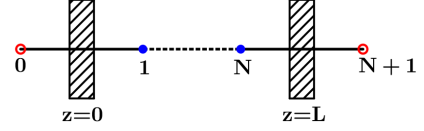

Fig. 3: Implementation of boundary conditions using fictitious image cells outside of the domain.

The model distinguishes between inlet and outlet boundaries as well as reflective walls. The importance of finite passage opening effects on performance has been addressed in a number of research studies [28]–[30]. To account for finite passage opening effects, a function tracks the overlap between the channel and the ports taking channel width into account. Assuming an isentropic change across the the step in cross section, one can formulate quasi-steady boundary equations for mass, momentum and energy [26] and solve the system of equations using wave and pathline compability equations [27]. This is done in a similar fashion to Paxson and Wilson [31]. The effect of this procedure on the formation of the shock waves is shown in Figure 4. Neglecting finite opening effects leads to an immediate formation of a right trevelling shock wave as soon as the wave rotor channel is exposed to an inlet port and a sudden drop in pressure as soon as the port closes, as shown in Figure 4(a). Including finite passage opening effects leads to a more gradual build up in pressure as the overlap increases. This is exemplified in Figure 4(b).

4) Source Terms Modelling: The friction source term assumes

$$\mathbf{S}_f = \begin{pmatrix} 0 \\ s_{f,2} \\ s_{f,3} \end{pmatrix} = \begin{pmatrix} 0 \\ -C_f \rho \dfrac{2f}{D_h} |u| u \\ \rho \dfrac{2f}{D_h} |u| c_p (T_w{-}T) - C_f \rho \dfrac{2f}{D_h} |u| u \dfrac{u_\theta}{u} \omega r \end{pmatrix} \tag{7}$$

where the friction factor is determined as a function of Reynolds number and hydraulic diameter and follows [27].

$$f = \begin{cases} \dfrac{0.25}{\left[\log_{10}\left(\dfrac{k}{3.7 D_h} + \dfrac{5.74}{Re^{0.9}} \right) \right]^2} & \text{for } 5000 \geq Re \geq 10^8 \\[2em] \dfrac{64}{Re_D} & \text{for } Re < 5000 \end{cases}$$

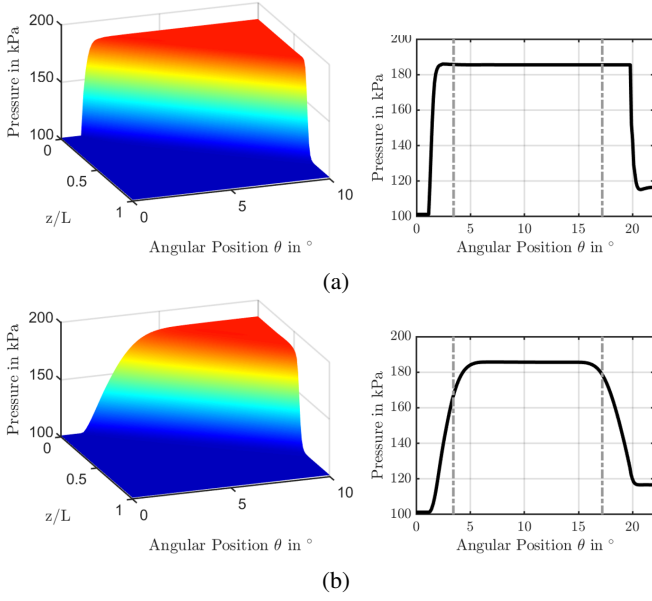where $Re_D = \dfrac{\rho u D_h}{\mu(T)}$

$$\tag{8}$$

Fig. 4: Formation of a shock wave without (a) and with (b) finite passage opening effects taken into account through the boundary conditions. The right hand plots illustrate static pressure within the channel at z/L=0 and the dashed grey line mark opening and closure of the port respectively.

Dynamic viscosity is assumed temperature dependant and computed using Sutherland's law. Equation 7 features the wall temperature T_w, which is a result of wall heat transfer and was approximated through a lumped capacitance model that follows a first-order differential equation, as given in Equation 9.

$$\frac{dT_w}{dt} = -\frac{1}{\tau}\left(T_w - T_i\right)$$
$$\text{with} \quad \tau = \frac{mc_p}{htcS} \tag{9}$$

where c_p refers to the specific heat capacity of the material, S the wetted surface of the wall passage and htc the convective heat transfer coefficient that was determined through Dittus-Boelter flat plate heat transfer correlation (Nu=0.0243$Re^{0.8}Pr^{0.4}$) and solved using Heun's method.

Inviscid profile forces are solved assuming the flow follows a meridional streamline along the curved channels. The corresponding source terms are given by

$$\mathbf{S}_v = \begin{pmatrix} 0 \\ s_{b,2} + s_{loss_{b,2}} \\ s_{b,3} + s_{loss_{b,3}} \end{pmatrix} = \begin{pmatrix} 0 \\ F_{b,z} + F_{loss,z} \\ (F_{b,\theta} + F_{loss,\theta})\omega r \end{pmatrix} \tag{10}$$

where the tangential force per unit volume is proportional to the change in tangential absolute velocity C_θ between two consecutive cells (see Figure 5) and can be stated as

$$F_{b,\theta} = \frac{\dot{m}}{V}\left(C_{\theta,o} - C_{\theta,i}\right) \tag{11}$$

In the model, the wall shape profile are defined through a

Bézier curve with the number and location of the control points being an input provided by the user. An example resulting in a symmetric camber is given in Figure 5.
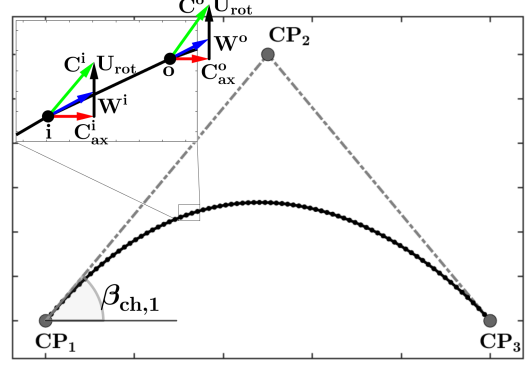

Fig. 5: Example of Bézier curve with three control points yielding a symmetric wall shape profile and detailed view of local velocity triangles at two consecutive nodes

To account for incidence losses and misalignment of the flow with the channel profile, an entropy based loss term (Δs =-$R \cdot \ln(1$-$\zeta_{loss})$) was introduced as

$$F_{loss,\theta} = \frac{\rho T |C_{ax}|}{|U|}\frac{\Delta s}{\Delta z} \tag{12}$$

The loss coefficient ζ is a function of rotational speed and was calibrated using experimental data [26]. The model includes the the port flow angles through applying the port flow angle at the image cell to include the effect of flow turning at from the port into the channel. Irreversibilites generated due to the port-channel flow turning are not directly accounted for, but implicitly contained within the ζ loss factor. Flow leakage occurs at either passage end at the rotor/stator interface and assumes the following form

$$\mathbf{S}_v = \begin{pmatrix} s_{lk,1} \\ 0 \\ s_{lk,3} \end{pmatrix} = \begin{pmatrix} -C_D\sqrt{\dfrac{2\gamma}{\gamma-1}}\left(\dfrac{\delta_{lk}}{H_{ch}\Delta z}\right)\sqrt{p\rho}\Phi \\ 0 \\ -C_D\sqrt{\dfrac{2\gamma}{\gamma-1}}\left(\dfrac{\delta_{lk}}{H_{ch}\Delta z}\right)h\sqrt{p\rho}\Phi \end{pmatrix} \tag{13}$$

where H_{ch} represents the channel height, δ_l the leakage gap and h the specific enthalpy. The discharge coefficient C_D is fixed at 0.64. The leakage function Φ is defined as

$$\Phi = \sqrt{\left(\frac{p_{\text{cav}}}{p}\right)^{2/\gamma} - \left(\frac{p_{\text{cav}}}{p}\right)^{(\gamma+1)/\gamma}}$$
$$\text{for} \quad \frac{p_{\text{cav}}}{p} > \left(\frac{2}{\gamma+1}\right)^{\gamma/(\gamma-1)}$$
$$\Phi = \sqrt{\left(\frac{2}{\gamma+1}\right)^{2/(\gamma-1)} - \left(\frac{2}{\gamma+1}\right)^{(\gamma+1)/(\gamma-1)}} \tag{14}$$
$$\text{for} \quad \frac{p_{\text{cav}}}{p} < \left(\frac{2}{\gamma+1}\right)^{\gamma/(\gamma-1)}$$

5) Submodels: The approach used to model leakage cavity pressure follows the correlations given by Paxson [32] and Fatsis [33]. The cavity pressure p_{cav} in Equation 14 is updated after every completed cycle using a lumped capacitance model, as given in the mass and energy balances shown in Equation 15. The leakage cavity is assumed to be perfectly sealed without any interaction with the ambience. The first-order system is integrated using an explicit Runge-Kutta scheme and yields cavity mass and temperature, which in combination with the equation of state exhibit cavity pressure for the current time step.

$$\frac{dm_{\text{cav}}}{dt} = A\Delta x \left(\sum_i s_{1,i}^l + \sum_i s_{1,i}^r \right)$$
$$\frac{d}{dt}(m_{\text{cav}}e_{\text{cav}}) = \dot{Q}_{\text{wht}} + A\Delta x \left(\sum_i s_{3,i}^l + \sum_i s_{3,i}^r \right) \quad (15)$$
$$\text{where} \quad e_{\text{cav}} = c_{\text{v}}T_{\text{cav}}$$

where the wall heat transfer term $\dot{Q}_{\text{wht}}$ was approximated through heat transfer from the rotor wall and the cavity temperature.

The combustor model links the high pressure charging zone (HPA and HPG ports) and is used to provide the corresponding boundary conditions, that is total pressure and temperature at the combustor outlet and static pressure at the inlet. It is implemented in a similar fashion to the leakage model. Temperature and mass in the combustor are determined from the following system of first-order equations, which is again integrated in time after each cycle is completed

$$\frac{dm_{\text{c}}}{dt} = \sum_i \dot{m}_i$$
$$\frac{d}{dt}(m_{\text{c}}e_{\text{c}}) = \dot{Q}_{\text{hr}} + \sum_i h_i \dot{m}_i \quad (16)$$
$$\text{where} \quad e_{\text{c}} = c_{\text{v}}T_{\text{c}}$$

$\dot{Q}_{\text{hr}}$ refers to the heat released through combustion. Combustor pressure can then again be inferred through the ideal gas equation. The additional mass due to fuel injection is neglected. The combustor inlet conditions are determined using Rayleigh flow relations that include an additional factor to account for cold flow pressure losses.

B. Baseline Wave Rotor

The baseline wave rotor considered throughout this study is a small-scale throughflow rotor with symmetrically cambered wall profiles, as displayed in Figure 6. The rotor is 60 mm in diameter, 30 mm in length and each channel is approximately 2.9 mm in width and 6 mm in height. Finally, the rotor houses 46 channels with a maximum profile angle of 21.5°. It was designed to provide approximately 400-500 W shaft power output at a peak cycle temperature of 750°C and peak total inlet pressure of 285 kPa at a design rotational speed of 32,000 rpm. The main geometric dimensions are summarised in Table I.

The corresponding port solution and expected main shock

and rarefaction waves are depicted in the schematic of Figure 7. During each cycle (θ_{cycl}=120°), the rotor passages are exposed to a high- and low pressure in- and outlet ports. While experimental testing on the rotor were done in an open loop configuration, the model connects the high pressure ports HPA and HPG through the steady-flow combustor model.
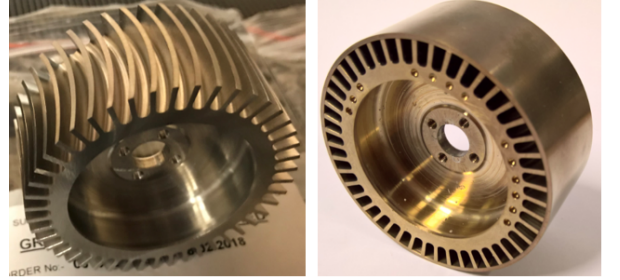

Fig. 6: Wave rotor turbine with symmetrically cambered profiles serving as a baseline model.

TABLE I: Dimensions of the Bath μ-wave rotor.

Dimensions Bath μ-Wave Rotor	
Rotor diameter [mm]	60
Number of channels	46
Channel shape	sym. cambered max. $|\beta_{ch}|$ = 21.5°
Channel length [mm]	30
Channel width [mm]	2.9
Channel height [mm]	6
Nominal clearance [mm]	variable 0.1 - 0.4
Number of cycles per revolution	3
Design rotational speed [rpm]	32,000

C. Discretisation Sensitivity Study

In order to ensure the results are independent of the discretisation length Δz of the cartesian grid, while computation time is kept to a minimum, a grid sensitivity study is performed. In the process, the number of cells n_z in the computational domain is varied 15 to 120 corresponding to a non-dimensional cell size $\Delta z/L$ ranging from 0.071 to 0.008. The results of this study are given in Figure 8 and reveal that for a cell count of 75 the relative error with respect to the maximum cell number investigated of 120 is within 2.3%. This appears to be an acceptable compromise between numerical accuracy and the required CPU time to reach a limit cycle.

D. Numerical Campaign

The main objective of this study is to characterise the behaviour and sensitivity of the wave rotor gas turbine to changes in operating conditions. To do so, the following parameters shall be considered; starting from the baseline rotor geometry given in Table I and the port solution shown
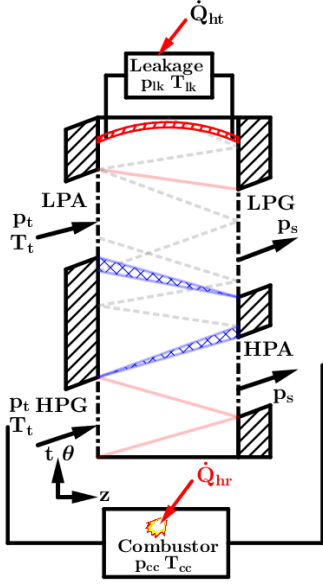
Fig. 7: Model schematic showing port arrangement and expected wave pattern for the treated four-port throughflow wave rotor turbine. The schematic further outlines the submodels used for leakage that is active at the ends of the rotor channel and the combustor that connects the high pressure ports HPG and HPA.
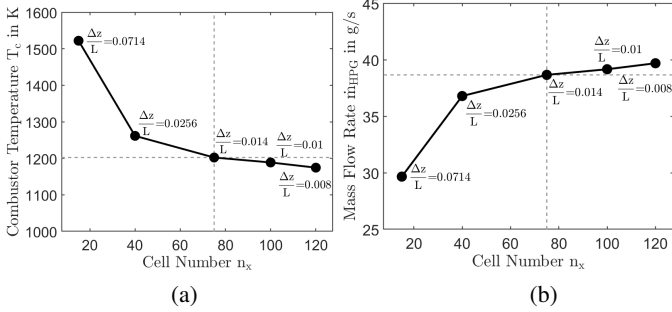

Fig. 8: Results of mesh sensitivity study for (a) combustor outlet temperature and (b) mass flow rate through the HPG port. Annotations show nondimensional cell size $\Delta z/L$. The dashed line show the results for n_z=75, which corresponds to the mesh size used for further simulations.

in Figure 7 the effect of heat release and loop flow ratio on dependant variables such as thermal efficiency, compression/expansion efficiency, shaft power output, combustor outlet temperature, pressure ratio and EGR/FAE rate shall be investigated. Furthermore, the influence of combustor pressure loss on the performance parameters is investigated as well. To do so, heat release is varied between 26 kW and 18 kW, while loop flow ratio is varied from 1.2 to 1.6. Loop flow ratio dictates scavenging of channels after opening of the LPA port. To vary loop flow ratio, it is assumed that pressurised air at 300 K is available. This of course would necessitate an upstream compressor, which ultimately would act as a parasitic load diminishing thermal efficiency. This

parasitic load is, however, not accounted in this study.

The next set of simulations examines how increased rotor/stator leakage and LPG backpressure influence wave rotor gas turbine behaviour. This is followed by a study on the consequences of increased and reduced wall profile camber on the dependant variables. To do so, the centre control point defining the wall contour (see Figure 3) is perturbed vertically to yield one case with lower blade camber (max.$|\beta_{ch}|$=15.7°) and one case with a higher camber (max.$|\beta_{ch}|$=27.3°) compared to the baseline profile. The final study considers a recuperated cycle as shown in Figure 9. To simplify the computations and point out the potential benefit of utilising exhaust gas temperature to preheat the combustor inlet temperature, it is estimated that the heat exchanger operates at 100 percent effectiveness, yielding $T_{t,HPA}$ equal to $T_{t,LPG}$. Flow through the recuperator will incur pressure losses, which is accommodated for through a 2% higher LPG backpressure than ambient.
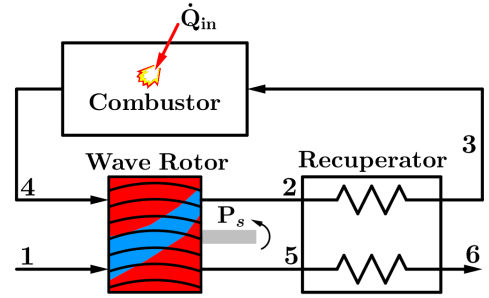

Fig. 9: Schematic including an additional heat recuperator utilising residual heat from the exhaust stream to preheat air before entering the combustor thus raising thermal efficiency at the cost of higher backpressure and pressure loss in the combustor loop.

All simulations commence from the same initial and boundary conditions. Wave rotor rotational speed is maintained at design speed of 32,000 rpm. Heat release is kept constant as well. To expedite the simulation and reach a limit cycle swiftly, where mass flow rates in the ports and temperatures and pressures in the leakage cavity and combustor are in steady-state, initial pressures and temperatures in the combustor and cavity are set to 250 kPa and 700°C, while thermodynamic conditions within the channel are set equal to ambient conditions (p=101.3 kPa and T=300 K).

E. Performance parameters

A summary of the range and scope of independant variables and the corresponding dependant variables examined in this study are given in Table II.

As stated previously, the loop flow ratio denotes the ratio of the high pressure and low pressure inlet massflow rates $\dot{m}_{HPG}/\dot{m}_{LPA}$. Compression pressure ratio and combustor pressure loss are defined as

TABLE II: Summary of independent and dependent variables used to characterise the wave rotor gas turbine.

Parameter	Unit	Range
Loop flow ratio λ	[mm]	1.2-1.6
Heat release $\dot{Q}_{hr}$	[kW]	14-26
Axial Leakage Gap δ_z	[mm]	0.1-0.35
LPG backpressure p_{LPG}	[kPa]	$p_\infty/1.0$-$p_\infty/0.90$
Combustor Pressure Loss $\Delta p_{\mathrm{HPG\text{-}HPA}}/p_{\mathrm{HPG}}$	[-]	0%-4%
max.$\vert\beta_{ch}\vert$	°	15.7-27.3
Combustor outlet temperature T_c	[K]	
Avg. rotor temperature T_w	[K]	
Shaft power output P_s	[W]	
Thermal efficiency η_{th}	[-]	
Compression/expansion efficiency $\eta_{c,x}$	[-]	
Pressure ratio Π_{TT}	[-]	
EGR rate Ψ_{EGR}/FAE rate Ψ_{FAE}	[-]	

$$\Pi_{TT} = \frac{p_{t,\mathrm{HPA}}}{p_{t,\mathrm{LPA}}}$$
$$\Delta p_c = 1 - \frac{p_{t,\mathrm{HPG}}}{p_{t,\mathrm{HPA}}} \tag{17}$$

Thermal efficiency is calculated using predicted shaft power output P_s and first law resulting in

$$\eta_{th} = \frac{P_s}{\dot{m}_{\mathrm{HPG}}\overline{c}_p(T_{\mathrm{HPA}} - T_{\mathrm{HPG}})} \tag{18}$$

Compression and expansion efficiency are determined splitting up hot and cold gas streams and taking EGR and FAE into account, as presented by Chan et al. [34] and taking heat internal heat transfer into account. The corresponding equations therefore read

$$\eta_c = \frac{\dot{m}_{\mathrm{LPA}}c_{p,c}\left(T_{\mathrm{HPA,c}}^{is}\text{-}T_{\mathrm{LPA}}\text{-}\Delta T_c\right)+\dot{m}_{\mathrm{EGR}}c_{p,h}\left(T_{\mathrm{HPA,h}}^{is}\text{-}T_{\mathrm{LPG}}\text{-}\Delta T_c\right)}{\dot{m}_{\mathrm{LPA}}c_{p,c}\left(T_{\mathrm{HPA,c}}\text{-}T_{\mathrm{LPA}}\right)+\dot{m}_{\mathrm{EGR}}c_{p,h}\left(T_{\mathrm{HPA,h}}\text{-}T_{LPG}\right)}$$
$$\eta_x = \frac{\dot{m}_{\mathrm{LPG}}c_{p,h}\left(T_{\mathrm{HPG}}\text{-}T_{\mathrm{LPG}}\text{-}\Delta T_x\right)+c_{p,c}\dot{m}_{\mathrm{FAE}}\left(T_{\mathrm{HPA}}\text{-}T_{\mathrm{LPG,c}}\text{-}\Delta T_x\right)}{\dot{m}_{\mathrm{LPG}}c_{p,h}\left(T_{\mathrm{HPG}}\text{-}T_{\mathrm{LPG}}^{is}\right)+c_{p,c}\dot{m}_{\mathrm{FAE}}\left(T_{\mathrm{HPA}}\text{-}T_{\mathrm{LPG,c}}^{is}\right)} \tag{19}$$

where ΔT_c and ΔT_x account for the heat transfer between hot and cold gas streams within the wave rotor [35]. Since the exact values for this is not known, it is assumed that they are equal. This is assumption becomes more accurate the closer loop flow ratio is to unity. In order to be able to solve the equation both compression and expansion efficiency are assumed to be equal $\eta_c = \eta_x$.

Furthermore, the equation takes mixing through EGR and FAE in the outlet ports into account. To compute EGR and FAE the interfaces between hot and cold gas flows are tracked at each cycle and time step using Equation 20

$$m^t = m^{t-1} + \Delta t u^{t-1}$$
$$\text{with } t = t^{t-1} + \Delta t \tag{20}$$

Since the channel geometry is discretised into a finite number of elements, u^{t-1} needs to be interpolated from the the two nodes closest to the position at time t. Equation 20 is evaluated for both inlet ports (HPG and LPA), which are finally terminated as soon as $z=L$ and give out the final interface position $\theta_{\mathrm{HPG,LPA}}^{\mathrm{int}}$. If $\theta_{\mathrm{LPA}}^{\mathrm{int}}$ is in between opening and closure of the HPA port, EGR rate can be evaluated. Similarly, in the case of $\theta_{\mathrm{HPG}}^{\mathrm{int}}$ being within the LPG port, FAE is present and can be calculated accordingly.

III. RESULTS AND DISCUSSION

A. Variation in Loop Flow Ratio and Heat Release

The effect of a variation in loop flow ratio own performance is given in Figure 10 depicting three contour plots of normalised static pressure (Fig. 10(a)) and normalised static temperature (Fig. 10(b)) for different flow ratios (λ=1.2, 1.4 and 1.6). The pressure contour reveals that the wave dynamics within the channel remains relatively stable in the depicted λ range. The temperature plots reveal that, as one approaches a loop flow ratio of unity, higher LPA inlet pressures are necessary in order to supply the required mass flow rate $\dot{m}_{\mathrm{LPA}}$. As a consequence, one can witness a greater penetration of cold flow into the channel and thus lower EGR rates. At constant heat release, higher loop flow ratio yields an increase in combustor outlet temperature, as can be seen comparing temperature contours for λ=1.2 and 1.6. Furthermore, due to the higher LPA inlet pressure the HPG port is faced with greater backpressure resulting in reduced hot air penetration length $L_{p,h}$ ultimately leading to an onset of FAE, as shown in the enhanced view in Figure 10(b). Overall, higher loop flow ratio results in higher combustor inlet temperature, which in turn gives a higher combustor outlet temperature for a given heat release rate.

Figure 11 presents estimates for shaft power output, thermal efficiency and combined compression/expansion efficiency as a function of loop flow ratio and combustor pressure loss for a fixed combustor pressure loss of 3%. The data indicate that the variation of predicted shaft power output with loop flow ratio is almost linear. Higher heat release increases total enthalpy reaching the wave rotor channels through the HPG port and thus results in increased extraction of torque. As a direct consequence of this, thermal efficiency appears to increase with lower loop flow ratio. In terms of compression/expansion efficiency higher heat release rates indicate greater adiabatic efficiency. In contrast to thermal efficiency, an increase in loop flow ratio appears to improve compression/expansion efficiencies. This may stem from a higher pressure ratio necessary to reach the limit circle as shown in Figure 12. The kink at 18 kW heat input and low loop flow ratios of 1.2 and 1.3 is a result of onset of FAE, which lowers the average LPG outlet temperature and results in an increase in compression/expansion efficiency.
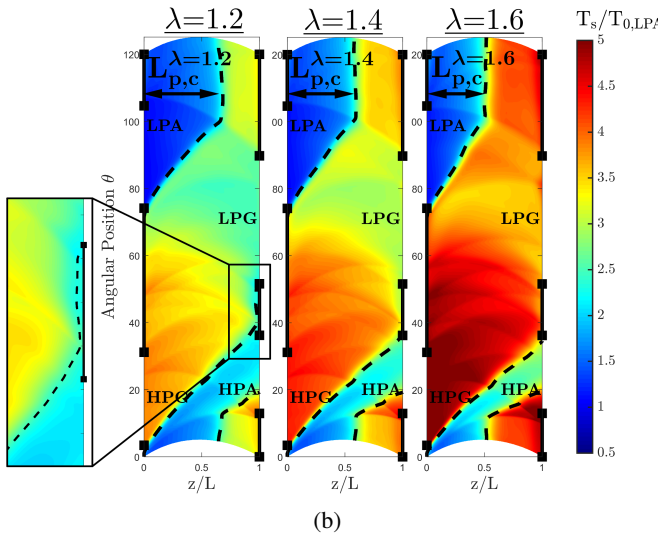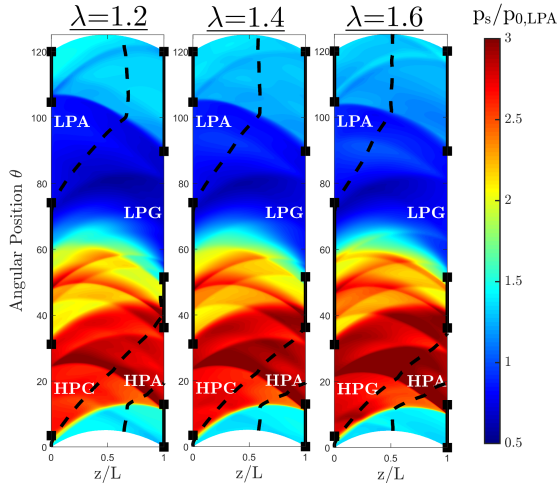
(a)

(b)

Fig. 10: Comparison showing (a) normalised static pressure and (b) normalised static temperature for three different loop flow ratios for a constant heat release. The pressure contour plots outline a relatively stable position of the shock and expansion waves with respect to the ports. The temperature field implies a reduction in cold air penetration length $L_{p,c}$ as well as an increase in maximum temperature within the computational domain as a consequence of increased EGR rate.

Nonetheless, FAE is undesired as it increases EGR and represents flow that is expelled unused.

Greater loop flow ratios represent a smaller fresh air mass flow rate and thus result in considerably higher combustor temperatures as given in Figure 12 for a given heat release rate. Estimated wall temperature remains approximately 400 K below the peak cycle temperature, reflecting the self-cooling capabilities of wave rotors. However, this can be expected to be a rather optimistic prediction, as the rotor is in direct contact with the internal leakage cavity, whose temperature at the limit cycle is above the values presented in Figure 12. Finally, the graphs present combustor mass flow
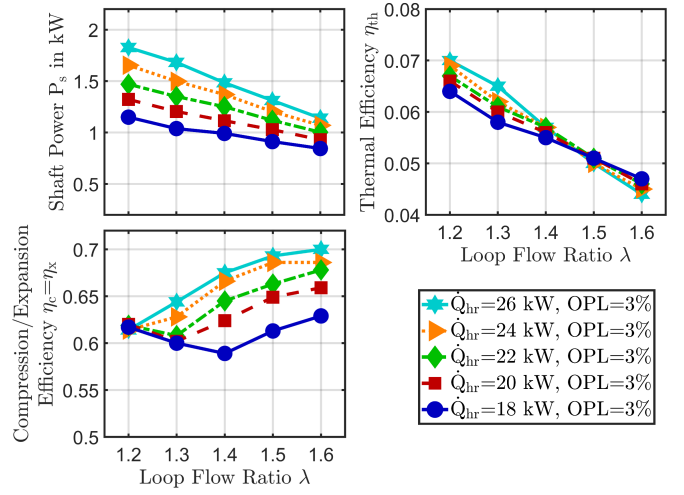

Fig. 11: Estimated effect of variation in loop flow ratio for various heat release rates and a fixed combustor OPL on shaft power, thermal- and compression/expansion efficiency.
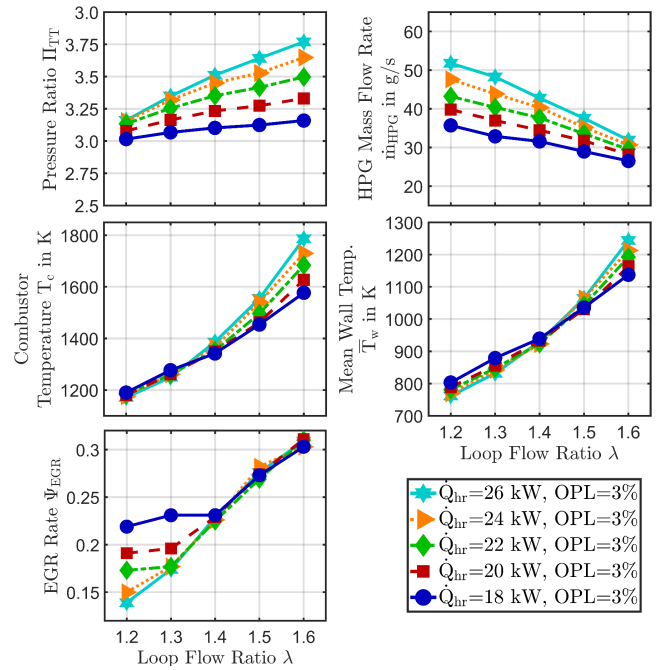

Fig. 12: Estimated distribution of (a) pressure ratio, combustor temperature and mean rotor wall temperature and (b) combustor loop mass flow rate and its associated EGR rate. Data are plotted against loop flow ratio and for a variety of heat release rates at constant combustor OPL.

rate $\dot{m}_{HPG}$, which increases the more fuel is injected and the higher the generated pressure ratio is.

The next step is to examine performance behaviour at constant loop flow ratio, as heat release and combustor pressure loss are varied. Obviously, pressure loss across the combustor cannot simply be altered for a given geometry and combustor type. However, the following results introduce the
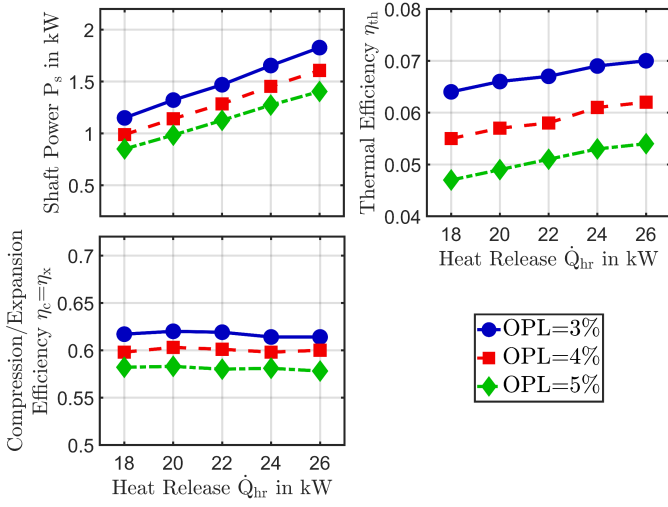
Fig. 13: Graphs outlining the effect of different combustor overall pressure losses with variation in heat release for shaft power, thermal efficiency and combined compression and expansion efficiency. Loop flow ratio is maintained at 1.2.
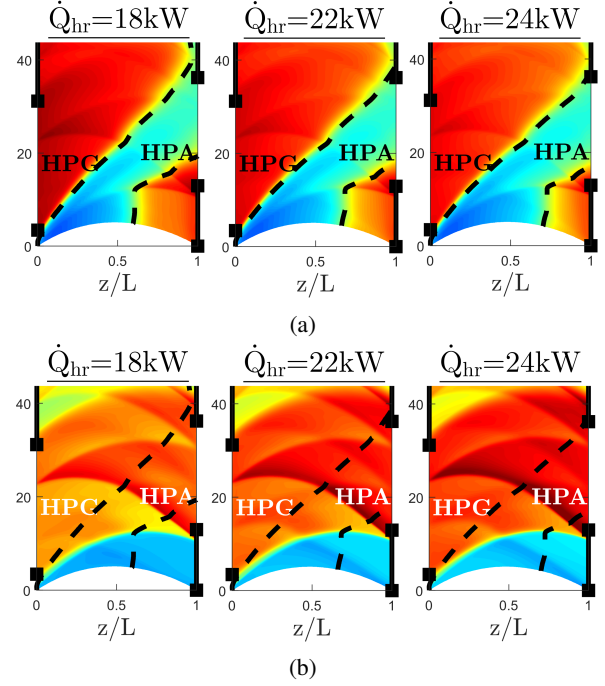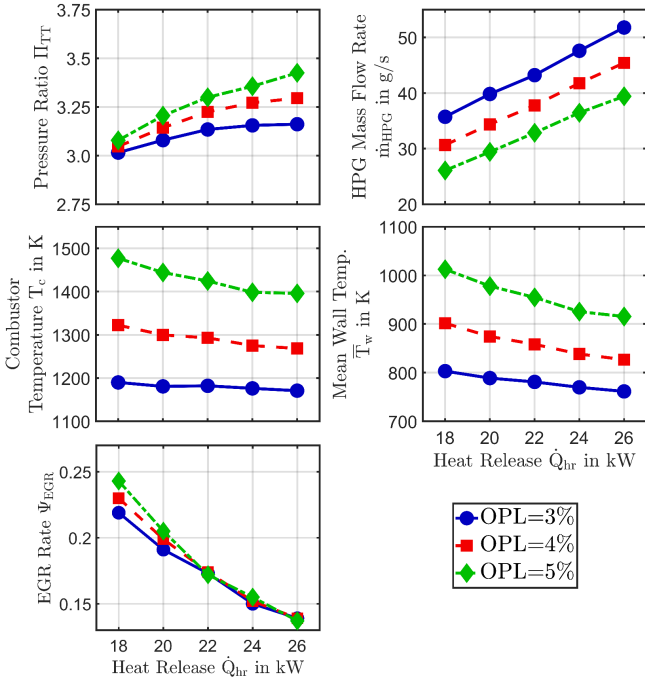

Fig. 14: Variation of estimates for (a) total-to-total pressure ratio, combustor temperature, average rotor wall temperature as well as for (b) combustor mass flow rate and EGR rate for three different combustor OPL.

potential benefits a low pressure loss combustor can offer. This can directly be witnessed examining Figure 13, which outlines benefits for generated torque, thermal efficiency as well as and combined compression/expansion efficiency. Higher combustor pressure loss necessitates a considerably higher pressure ratio and combustor outlet temperature in order to reach the limit cycle, as given in Figure 14.

(a)

(b)

Fig. 15: Contour plots for (a) normalised static pressure and (b) normalised static temperature. The position of primary and secondary shock waves remains relatively stable. The temperature contour indicates the effect of variation in heat release rate on the location of the fresh air stream at the HPA port. Reducing heat release signifies a reduction in combustor mass flow rate and thus lower hot gas penetration length $L_{p,h}$. Further reduction in heat release will lead to the onset of FAE.

Depending on the rotor material chosen, higher pressure losses can thus lead - despite rotor self cooling capabilities - to average wall temperatures exceeding thermal limits and thus have a knock-on effect on service life. Low pressure losses however imply reduced thermal stresses and therefore allow to resort to less temperature resilient and thus more cost effective rotor materials. Despite lower pressure ratio with a decreased OPL, the reduced combustor outlet temperature of approximately 200 K between OPL=3% and OPL=5% accounts for higher density and as a result larger mass flow rates through the HPG port varying between approximately 36 g/s to 52 g/s at OPL=3%. The lowest predicted EGR rate for all OPL occurs for higher heat release and gradually increases as heat release is decreased. The reason for this is exemplified in the temperature contours of Figure 15(a) showing the high pressure zone of HPG and HPA ports. At higher heat input higher combustor mass flow rates ensure sufficient scavenging of channels. Reducing injected fuel flow rate and thus heat release yields lower combustor mass flow rates entering through the HPG port. This reduces $L_{p,h}$ until a portion of the cold, compressed stream does not reach the HPA port, but is carried over and expelled as FAE through the LPG port. This behaviour is illustrated in the contour plots at $\dot{Q}_{hr}$=18 kW and in the

EGR and combustor temperature at OPL=5% in Figure 14. Although variation in heat release rate constitute higher mass flow rates through the channels, the overall wave dynamics and shock wave distribution does not appear to vary significantly, as illustrated in Figure 15(b).
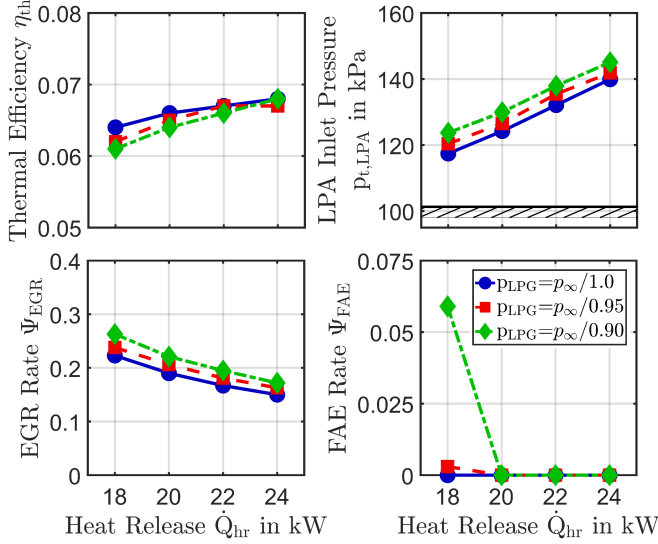

Fig. 16: Effect of exhaust backpressure on thermal efficiency, LPA inlet pressure, EGR and FAE rate as heat input is varied. Data were gathered for a constant loop flow ratio of 1.2 and constant combustor pressure loss of 3%.

B. Exhaust Backpressure

Employing the wave rotor in combination with a recuperator or a power turbine located downstream of the exhaust outlet port (LPG), inevitably increases backpressure experienced by the wave rotor. The implications of such a variation in boundary conditions are treated in Figure 16 for three different levels of backpressure ranging from ambient conditions (p_∞) to rather large levels of 11% higher than ambient. Interestingly, the effect of this proves negligible for predicted shaft power output, combustor temperatures and mass flow rates. Albeit rather small, one can note a gentle decrease in estimated thermal efficiency, in particular visible at lower heat input. As expected, for a given loop flow ratio the delivery pressure necessary to maintain a particular low pressure mass flow rate will increase the higher the backpressure exerted through the LPG port, as given in the top right hand side graph of Figure 16. Similar as seen before, EGR rate gradually increases as heat release rate is reduced. In this scenario, EGR rate proves approximately five percentage points lower when comparing ambient pressure at LPG to the maximum imposed backpressure of $p_\infty/0.90$. Finally, while moderate backpressures exhibit mere hints of FAE onset, large backpressure appear to promote undesirable FAE rates sooner.

C. Axial Leakage Gap

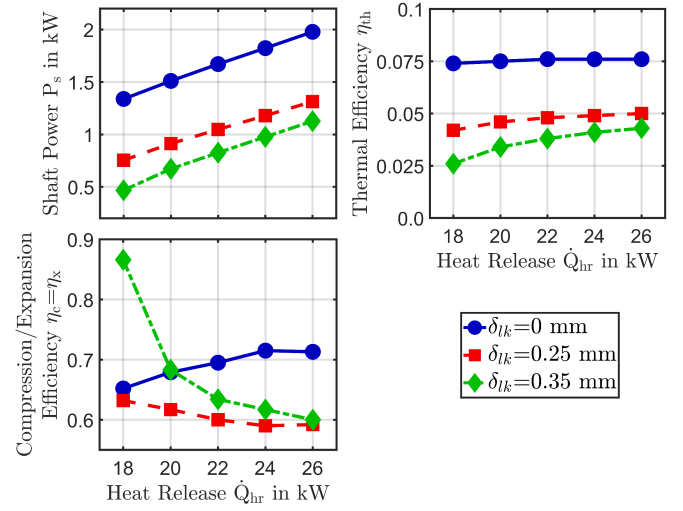Figure 17 illustrates a comparison of estimated shaft power, thermal efficiency and compression/expansion effi-

Fig. 17: Impact of axial leakage variation from a theoritcal ideal of 0 mm to up to 0.35 mm on predicted shaft power output, thermal efficiency and compression/expansion efficiency.
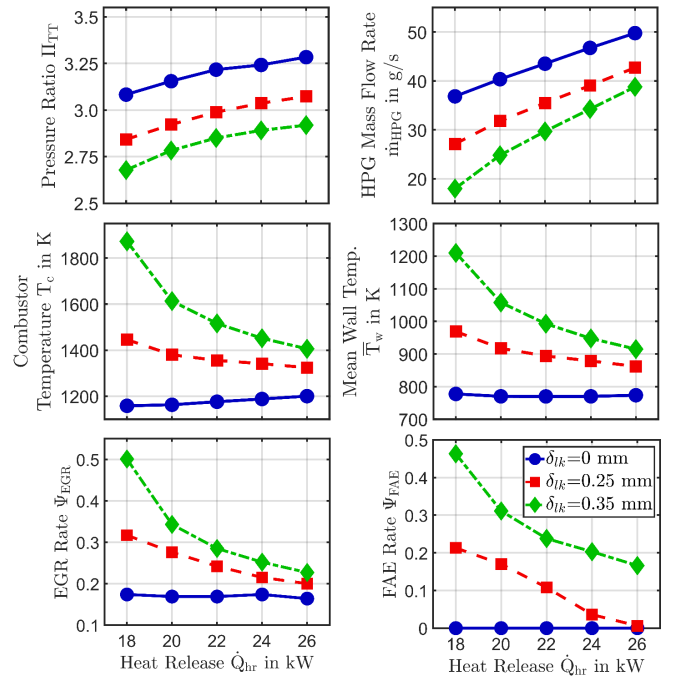

Fig. 18: Graphs indicating the implications of various axial leakage distances on (a) pressure ratio, combustor outlet temperature and average rotor wall temperatures, as well (b) combustor mass flow rate, EGR and FAE rates.

ciency for three different axial leakage gaps at constant loop flow ratio of λ=1.2. The simulation data confirms a significant impact on wave rotor gas turbine performance. As one approaches the theoretical limit of 0 mm both torque output and thus thermal efficiency increase considerably up to approximately 8%. Also, compression/expansion efficiency benefit from lower leakage with maximum values of 70%.

The strong increase towards lower heat release rates for the maximum investigated leakage distance, is rooted in an excessive amount of EGR and FAE, similarly to the one noted in Figure 11 and 12. Associated with the high compression/expansion efficiencies at low leakage is a large pressure ratio of up to 3.25, which decreases to below 3 for higher leakage, as given in Figure 18.

At the limit cycle for high axial leakage, there appears to be an unacceptably high demand for combustor outlet temperature at approximately 1800 K, while the peak cycle temperature for moderate leakages ranges in between 1100 to 1400 K. This implies average wall temperatures below 1000 K. As increased rotor-stator distances promote higher leakage flows from the ports/channels into the leakage cavity the net mass flow rates through the combustor decreases accordingly compared with lower leakage cases. This is shown in Figure 18. As already indicated through the compression/expansion efficiencies, high leakage gaps foster higher EGR and FAE rates as given in the centre and right hand side graphs of Figure 18. This is primarily caused as leakage mass flow rates increases relative to to overall port mass flow rates, which compromises scavenging capabilities.
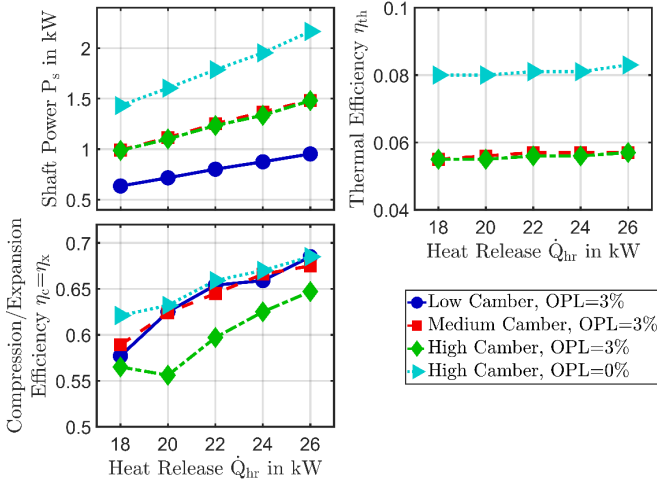
D. Wall Camber

Fig. 19: Effect of different wall camber and heat input angles on shaft power, thermal efficiency and compression/expansion efficiency. Low, medium and high camber designs are compared at constant combustor pressure loss OPL=3%. results for a theoretical design with zero combustor pressure are presented as well.

In order to examine the effect of wall camber, three levels of symmetrically cambered wall profiles were investigated at constant loop flow ratio of 1.2 and OPL=3%. In addition, the high wall camber case was run at zero overall pressure loss, indicating the effect of pressure gain combustion on the performance variables. The results for shaft power, thermal efficiency and compression/expansion efficiency are given in Figure 19.

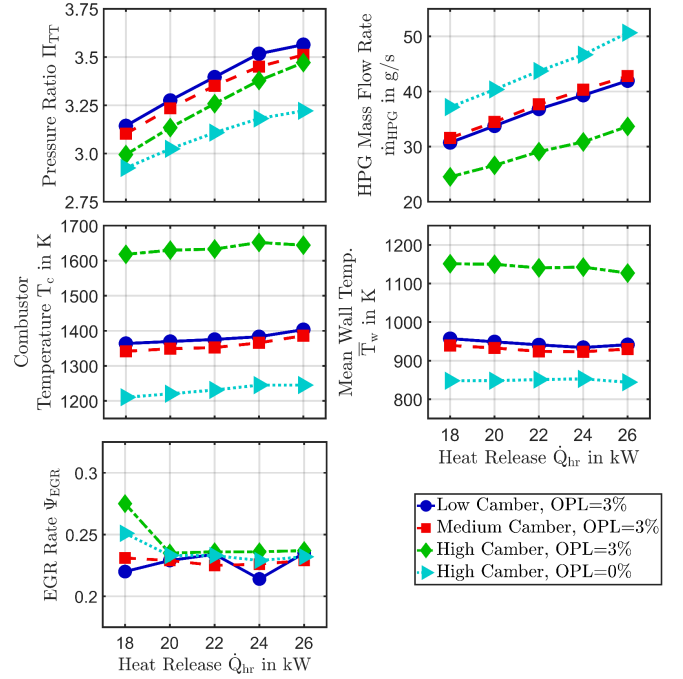As lower camber signifies reduced momentum transfer, the

Fig. 20: Simulation results comparing distributions for (a) pressure ratio, combustor temperature and mean rotor wall temperature, and (b) combustor mass flow rate and EGR rate at constant loop flow ratio of 1.2 .

low camber case features low levels of generated torque and thermal efficiency compared with higher camber geometries. However, compression and expansion efficiency remain at a reasonably high level between approximately 60% and 70%. Interestingly, medium and and high camber designs feature comparable levels of shaft power and thus thermal efficiency levels of approximately 6%, which is a result of higher combustor outlet temperature and lower mass flow rate as given in Figure 20. However, if one were to employ a combustor not being subject to pressure losses, thermal efficiency can be further advanced to 8%. The reason for this is that lower pressure losses enables mass flow rates to recover beyond the level of medium and low camber at OPL=3%. In addition, combustor temperatures are significantly reduced. These results emphasise the findings shown in Figure 14 and 15 stating the importance of a low pressure loss combustor design or the application of pressure gain combustion.

E. Heat Recuperation

The final test deals with the potential of employing a recuperator that uses exhaust energy to preheat the charge air upstream of the combustor. Despite the advantage of reducing the necessary heat input for a given temperature difference between HPA and HPG port, one needs to account for an increase in total pressure loss across the combustor loop and increased back pressure at the LPG port. In addition, loop flow ratio needs to be sufficiently low in order to guarantee EGR rates are reasonably low and thus mixed-
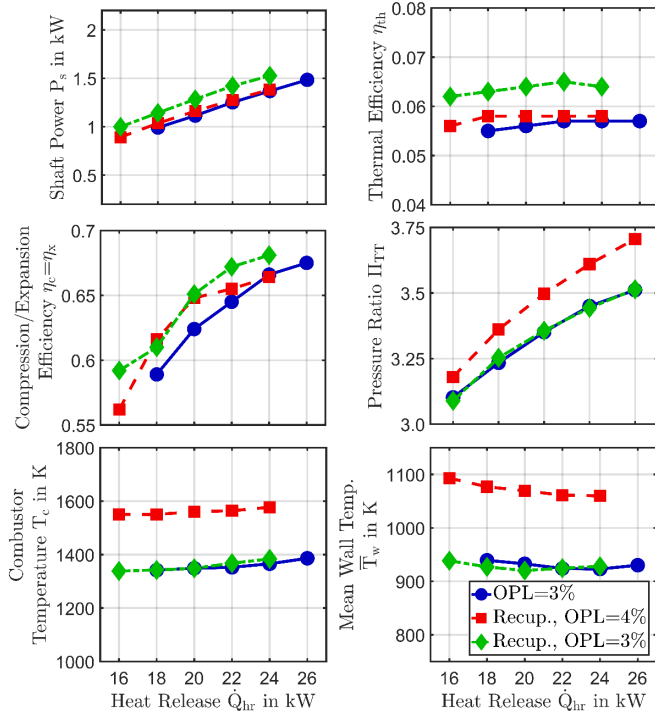
Fig. 21: Variation of predicted shaft power, thermal efficiency, compression/expansion efficiency as well as pressure ratio, combustor outlet temperature and mean rotor wall temperature for unrecuperated (λ=1.4, OPL=3%) and recuperated designs (λ=1.4, OPL=3% and OPL=4%).

out HPA temperatures remain below temperature in the LPG port. The air-to-air heat exchanger effectiveness is assumed to be unity.

Comparing an unrecuperated case with a fixed combustor pressure loss of 3% and loop flow ratio of 1.4 with two recuperated cases with OPL=3% and OPL=4% respectively and an increased backpressure at the LPG port of $p_\infty/0.98$ yields the results illustrated in Figure 21. Examining both shaft power and thermal efficiency graphs, it transpires that for a higher combustor loop pressure loss the recuperated machine cannot yield an improvement. This is mainly a consequence of a relatively small temperature difference between the temperatures in the HPA and LPG port of approximately 30-40 K and the penalty incurred by increased pressure losses. If one were to assume a similar combustor pressure loss, then a thermal efficiency benefit could be witnessed. As a result, it can be concluded that the application of a recuperator in the presented scheme is not desirable and will likely incur higher losses than without heat recuperation. In addition, it is noteworthy that the interaction of hot and cold streams within the wave rotor channels itself already acts as internal recuperation, which limits the additional benefit of an external air-to-air heat exchanger.

IV. CONCLUSIONS AND OUTLOOK

In this paper a quasi-one-dimensional wave action model was used to assess the performance of a micro gas turbine that employs a wave rotor turbine with cambered wall profiles for shaft power extraction. A parametric study was conducted aimed at identifying key performance parameters. To conclude, the main findings of the study can be summarised as follows:

- Estimated compression/expansion efficiencies throughout the study vary within approximately 60 to 70 % indicate the virtue of shock wave compression and expansion.
- The simulation results for thermal efficiency prove to be rather low at around 6-7%. This is owed to the nature of torque extraction, which occurs in a pulsatile manner and is thus less efficient compared to crypto-steady turbomachines. However, the presented wall profile is a simple, symmetrical arc that may not represent the ideal shape for torque generation. Also, in combination with low pressure loss combustors or pressure-gain combustors higher system efficiencies may be achievable.
- Increased profile camber results in greater torque extraction. However, for a given combustor pressure loss there appears to be a limit in camber at which combustor temperature reaches an unacceptably high level at the limit cycle and thus resulting in low mass flow rates and compromised system efficiencies.
- Leakage is a primary performance parameter that needs to be kept at a minimum in order to achieve acceptable and stable operating conditions.
- A loop flow ratio towards unity appears favourable in terms of shaft power output and thermal efficiency. In the event that no upstream pressurisation is used, this is limited by ambient stagnation properties, resulting in loop flow ratios of approximately 1.5 to 1.6 for the presented design.
- The simulation results suggest the application of an external air-to-air recuperator does not lead to a performance benefit. Any reduction in required heat input in the combustor is offset by an increase in pressure losses and higher exhaust backpressure. In addition, direct contact between hot and cold gas streams within wave rotor channels act as internal heat recuperation upstream, therefore limiting the effect of an additional external heat exchanger.

REFERENCES

[1] Special Interest Group, Robotic & Autonomous Systems, "RAS 2020 Robotics and Autonomous Systems," The Knowledge Transfer Network, July 2014.

[2] Defence Science and Technology Laboratory. Competition Document: Beyond Battery Power. DSTL. Accessed: 2017-Nov-10. [Online]. Available: https://www.gov.uk/government/publications/cde-themed-competition-beyond-battery-power/competition-document-beyond-battery-power

[3] T. Verstraete, Z. Alsalihi and R. A. Van den Braembussche, "Numerical Study of the Heat Transfer in Micro Gas Turbines," *J. Turbomach*, vol. 129, no. 4, pp. 835–841, 2007.

[4] A. Marcellan, W.P.J. Visser and P. Colonna, "Potential of Micro Turbine Based Propulsion Systems for Civil UAVs: A Case Study," in *ASME Turbo Expo 2016: Turbomachinery Technical Conference and Exposition Volume 1: Aircraft Engine; Fans and Blowers; Marine*, 06 2016, p. V001T01A031.

[5] R.A. Van den Braembussche, "Micro Gas Turbines - A Short Survey of Design Problems," Neuilly-sur-Seine, France: RTO, Educational Notes RTO-EN-AVT-131, 2012.

[6] M.J. Vick, "'High Efficiency Recuperated Ceramic Gas Turbine Engines for Unmanned Air Vehicle Propulsion," PhD Thesis, Imperial College London, 2012.

[7] N. Müller and L.G. Fréchette, "Performance Analysis of Brayton and Rankine Cycle Microsystems for Portable Power Generation," in *Proceedings of IMECE2002 ASME International Mechanical Engineering Congress & Exposition*, 11 2002.

[8] A.J. Head and W.P.J. Visser, "Scaling 3-36kW Microturbines," in *ASME Turbo Expo 2012: Turbine Technical Conference and Exposition Volume 5: Manufacturing Materials and Metallurgy; Marine; Microturbines and Small Turbomachinery; Supercritical CO2 Power Cycles*, 06 2012, pp. 609–617.

[9] S. Tüchler and C.D. Copeland, "Experimental Results from the Bath -Wave Rotor Turbine Performance Tests," *Journal of Energy Conversion and Management*, vol. 189, pp. 33–48, 3 2019.

[10] L. Pohořelský, P. Sané, T. Rozsas, N. Müller, "Wave Rotor Design Procedure for Gas Turbine Enhancement," in *Proceedings of the ASME Turbo Expo 2008*, ser. ASME Turbo Expo 2008: Power for Land, Sea, and Air, vol. 1. American Society of Mechanical Engineers, 2008, pp. 847–860.

[11] A. Fatsis, "Performance Enhancement of One and Two-Shaft Industrial Turboshaft Engines Topped With Wave Rotors," *International Journal of Turbo & Jet-Engines*, vol. 35, no. 2, pp. 137–147, 2018.

[12] M.R. Mataczynski, M.J. McClearn, F.R. Schauer, D.E. Paxson, D.E and J.L. Hoke, "Design and Testing of a Small Pressure Wave Supercharger for an Industrial Diesel Engine," *AIAA SciTech Forum - 55th AIAA Aerospace Sciences Meeting*, 2017.

[13] J. Li, E. Gong, L. Yuan, W. Li and K. Zhang, "Experimental Investigation on Pressure Rise Characteristics in an Ethylene Fuelled Wave Rotor Combustor," *Energy & Fuels*, vol. 31, no. 9, pp. 10 165–10 177, 2017.

[14] H.D. Perkins and D.E. Paxson, "Summary of Pressure Gain Combustion Research at NASA," *NASA/TM2018-219874*, 2018.

[15] J. Li, E. Gong, L. Yuan, W. Li and K. Zhang, "Experimental Investigation on Flame Formation and Propagation Characteristics in an Ethylene Fuelled Wave Rotor Combustor," *Energy & Fuels*, vol. 32, no. 2, pp. 2366–2375, 2018.

[16] J. Zhao and D. Hu, "An Improved Wave Rotor Refrigerator Using an Outside Gas Flow for Recycling the Expansion Work," *Shock Waves*, vol. 27, no. 2, pp. 325–332, 2017.

[17] D. Hu, Y. Yu, P. Liu, X. Wu and Y. Zhao, "Improving Refrigeration Performance by Using Pressure Exchange Characteristic of Wave Rotor," *Journal of Energy Resources Technology, Transactions of the ASME*, vol. 141, no. 2, 2019.

[18] H.E. Weber, *Shock Wave Engine Design*. New York: John Wiley & Sons, 1996.

[19] R.D. Pearson, "A Gas Wave-Turbine Engine Which Developed 35 HP and Performed Over a 6:1 Speed Range," in *Proceedings ONR/NAVAIR Wave Rotor Research and Technology Workshop*. Naval Postgraduate School, 1985.

[20] ——, "Pressure Exchangers and Pressure Exchange Engines," in *The Thermodynamics and Gas Dynamics of Internal-Combustion Engines, Volume II*, J.H. Horlock and D.E. Winterbone, Ed. New York: Oxford University Press, 1986, ch. 16, pp. 903–943.

[21] A. Mathur, "Design and Experimental Verification of Wave Rotor Cycles," in *Proceedings ONR/NAVAIR Wave Rotor Research and Technology Workshop*. Naval Postgraduate School, 1985.

[22] R. Taussig, P. Cassady, J. Zumdieck, W. Thayer and E. Klostermannt, "Investigation of Wave Rotor Turbofans for Cruise Missile Engines," Final Report Submitted by MSNW to DARPA, Tech. Rep., 1983.

[23] J. Piechna, "Feasibility Study of the Wave Disk Micro-Engine Operation," *J. Micromech. Microeng.*, vol. 16, 2006.

[24] J. Piechna and D. Dyntar, "Numerical Investigation of the Wave Disk Micro-Engine Concept," *International Journal of Gas Turbine, Propulsion and Power Systems*, vol. 2, no. 1, 2008.

[25] ——, "Hybrid Wave Engine Concept and Numerical Simulation of Engine Operation," *The Archive of Mechanical Engineering*, vol. LVII, no. 1, 2010.

[26] S. Tüchler and C.D. Copeland, "Validation of a Numerical Quasi One-Dimensional Model for Wave Rotor Turbines with Curved Channels," *J. Eng. Gas Turbines Power.*, GTP-19-1313.

[27] D.E. Winterbone and R.J. Pearson, *Theory of Engine Manifold Design: Wave Action Methods for IC Engines*. London and Bury St Edmunds, United Kingdom: Professional Engineering Publishing Limited, 2000.

[28] S. Eidelmann, "The Problem of Gradual Opening in Wave Rotor Passages," *Journal of Propulsion and Power*, vol. 1, no. 1, pp. 23–28, 1985.

[29] ——, "Gradual Opening of Skewed Passages in Wave Rotors," *Journal of Propulsion and Power*, vol. 2, no. 4, pp. 379–381, 1986.

[30] L.M. Larosiliere, "Three-Dimensional Numerical Simulation of Gradual Opening in a Wave Rotor Passage," *AIAA-93-2526*, 1993.

[31] D. Paxson and J. Wilson, "An Improved Numerical Model for Wave Rotor Design and Analysis," *AIAA*, Jan. 1993.

[32] D.E. Paxson, "A Numerical Model for Dynamic Wave Rotor Analysis," *AIAA-95-2800*, 1995.

[33] A. Fatsis, M. Vrachopoulos, S. Mavrommatis, A. Panoutsopoulou and F. Layrenti, "A Computational Method for Pressure Wave Machinery to Internal Combustion Engines and Gas Turbines," vol. 52, 04 2006, pp. 49–58.

[34] S. Chan, H. Liu and F. Xing, "Defining the Thermodynamic Efficiency in a Wave Rotor," *J. Eng. Gas Turbines Power*, vol. 140, no. 11, pp. 112 601–1–112 601–11, 2016.

[35] J. Wilson, G.E. Welch and D.E. Paxson, "Experimental Results of Performance Tests on a Four-Port Wave Rotor," *NASA/TM2007-214488*, 2007.